


Video-rate high-precision time-frequency multiplexed 3D coherent ranging

Ruobing Qian¹, Kevin C. Zhou ¹, Jingkai Zhang¹, Christian Viehland¹, Al-Hafeez Dhalla¹ & Joseph A. Izatt ^{1,2}✉

Frequency-modulated continuous wave (FMCW) light detection and ranging (LiDAR) is an emerging 3D ranging technology that offers high sensitivity and ranging precision. Due to the limited bandwidth of digitizers and the speed limitations of beam steering using mechanical scanners, meter-scale FMCW LiDAR systems typically suffer from a low 3D frame rate, which greatly restricts their applications in real-time imaging of dynamic scenes. In this work, we report a high-speed FMCW based 3D imaging system, combining a grating for beam steering with a compressed time-frequency analysis approach for depth retrieval. We thoroughly investigate the localization accuracy and precision of our system both theoretically and experimentally. Finally, we demonstrate 3D imaging results of multiple static and moving objects, including a flexing human hand. The demonstrated technique achieves submillimeter localization accuracy over a tens-of-centimeter imaging range with an overall depth voxel acquisition rate of 7.6 MHz, enabling densely sampled 3D imaging at video rate.

¹Department of Biomedical Engineering, Duke University, Durham, NC 27708, USA. ²Department of Ophthalmology, Duke University Medical Center, Durham, NC 27710, USA. ✉email: joseph.izatt@duke.edu

Real-time high-resolution three-dimensional (3D) imaging is highly desirable in a wide range of established and emerging fields including biomedical imaging, robotics, virtual/augmented reality, 3D printing, and autonomous vehicles. A useful distinction can be made between 3D volumetric imaging systems, which acquire fully sampled 3D tomographic data, versus 3D surface imaging or ranging systems which detect the depth range for every pixel in a 2D scene. The former are commonly used in medical imaging, whereas the latter, often collectively referred to as light detection and ranging (LiDAR), are of intense current interest primarily motivated by autonomous systems development. Optical coherence tomography (OCT) is a volumetric 3D imaging technique which has had great success in medical imaging, especially in ophthalmology^{1,2}. To date, OCT has primarily been developed for applications requiring micrometer-scale resolution and millimeter-scale imaging range. Recently, swept-source OCT (SSOCT) systems using lasers sweeping at 100's of kHz to MHz repetition rate have enabled fully sampled 3D volumetric imaging with several millimeters imaging range at 10 s of volumes/sec³. Frequency-modulated continuous wave (FMCW) LiDAR shares the same working principle as SSOCT, but prioritizes imaging range and high speed over axial resolution, and employs some form of surface detection (typically peak reflector position) to collapse the depth dimension to a single depth range measurement^{4,5}. As a coherent-based imaging technology, FMCW LiDAR offers high-precision 3D imaging with superior sensitivity and high immunity to ambient light.

One of the major challenges in FMCW LiDAR is extending the imaging range, which is determined by the instantaneous coherence length of the source and thus inversely related to the instantaneous linewidth. There is substantial current interest and effort in both the FMCW and OCT communities to increase the imaging range to the meter scale, of primary interest for room-scale robotic vision, and even multi-meter scale, which is of interest for autonomous vehicles. Multiple laser techniques have previously been demonstrated to decrease the instantaneous linewidth, such as vertical-cavity surface emitting lasers (VCSEL)^{6–11}, Fourier-domain mode locking (FDML)¹², optical time-stretching^{13,14}, single or stitched distributed feedback (DFB)^{15,16} and akinetic all-semiconductor programmable lasers¹⁷. These techniques have enabled extensions of the OCT imaging range from several centimeters to 1.5 m, and FMCW ranging with an imaging range up to several meters. However, increasing the imaging range in either technique without sacrificing depth resolution, using existing approaches, requires either a commensurate increase in receiver bandwidth or in acquisition time. Even with the fastest available photodetectors and digitizers, several seconds to hours have been required to acquire single volumes with hundreds of sampling points in each lateral dimension and tens of centimeters imaging range^{8,11,15,17}.

Another major challenge in FMCW LiDAR is the limited scanning speed, cost, and reliability of mechanical scanners. Traditional mechanical scanners, such as galvanometer mirrors and micro-electromechanical system (MEMS) scanners, have a maximum scanning rate of several kHz, which ultimately limits the line-scanning rate of both FMCW and ToF LiDAR. For these reasons, an emerging consensus in the LiDAR community is that compact, nonmechanical beam scanners with no moving parts are required for high speed imaging. For example, optical phased arrays (OPA) achieve beam steering by controlling the relative phase of arrays of coherent optical emitters^{18–20}, and thus allow compact solid-state LiDAR with MHz beam scanning bandwidths^{21,22}. However, the beam steering performance of OPA degrades with substantial spatial sidelobes as the wavelength sweeps²³. Another approach is to use diffractive optics to achieve

spectrally encoded spatial scanning. For example, Jiang et al. demonstrated a ToF LiDAR utilizing a discrete time-stretched broadband source and a grating for scanning²⁴. Riemensberger et al. demonstrated a massively parallel FMCW LiDAR system using a frequency comb laser combined with a grating for fast-axis scanning and 30 parallel detection channels⁴. All these works require complex laser design and system architecture. Most recently, Okano et al. demonstrated a swept source FMCW ranging system using a tunable VCSEL laser and a diffraction grating for beam scanning²⁵. However, this system still required several thousand spectral sampling points for each depth measurement, and thus only 30–45 distinct depth measurements were obtained along the grating scan axis. This limited the overall 3D voxel acquisition rate to 13.5–300 kHz, which is insufficient to support real-time densely sampled imaging operation.

Here, we report a time-frequency multiplexed FMCW LiDAR technique for high-speed high-precision 3D imaging using an akinetic all-semiconductor swept source, a diffraction grating for fast-axis beam steering, and a compressed sampling approach. In particular, we take advantage of the inherent sparsity of 3D ranging in the axial dimension, assuming that each lateral location contains only one dominant reflector in depth. Given this sparsity constraint, we show that we can reconstruct depth maps with higher precision and accuracy while using many fewer spectral points taken over a smaller bandwidth than the coherence length associated with that bandwidth. Using this optimized time-frequency analysis approach, we achieved sub-millimeter localization accuracy and precision using only 200 spectral points across a narrow bandwidth of 1.56 cm^{-1} for each depth measurement. A total of 475 depth measurements along the grating axis were obtained within a single laser sweep, generating an overall depth voxel acquisition rate of 7.6 MHz. We further studied the lateral and axial localization precision and accuracy of our system both theoretically and experimentally. Finally, we show real-time 3D imaging results of various everyday objects including a living human hand, with a maximum imaging range of 32.8 cm and a 3D frame rate as high as 33.2 Hz.

Results

Time-frequency multiplexed FMCW LiDAR system design.

The schematic of the sample arm optical design is shown in Fig. 1a, along with zoomed-in views of the Zemax (Kirkland, WA) optical model in Fig. 1b, c. An akinetic all-semiconductor programmable swept laser source (Insight Photonics Solutions; Lafayette, CO) centered at 1316 nm was used (detailed in the “Methods” section). A collimated beam created by a reflective collimator was focused by a $f = 2\text{ m}$ imaging lens. A galvanometer mirror was inserted before the imaging lens to accomplish beam scanning along the slow (vertical) axis, while a transmissive grating was placed immediately after the lens to achieve spectrally encoded scanning along the fast (horizontal) axis. The detailed optical design is described in the “Methods” section. The system achieved a horizontal FOV of 22.4 cm and diffraction limited performance with a lateral resolution of $890\text{ }\mu\text{m}$ at the focus along the grating direction (Fig. 1d–f). The vertical FOV was determined purely by the scanning angle of the galvanometer mirror; a vertical FOV of 12–20 cm was used in this work. The overall system design is shown in Fig. 1g. We employed a spectrally balanced interferometer topology incorporating three 50/50 2×2 fiber couplers (Thorlabs; Newton, NJ)²⁶, and the interferometric signal was detected using a balanced photodetector (Insight Photonics Solutions; Lafayette, CO) with 400 MHz bandwidth and digitized at 800 MS/s (Alazar Technologies; Pointe-Claire, QC, Canada). A total of 47,646 samples were collected per sweep. The maximum imaging range of the system is determined by

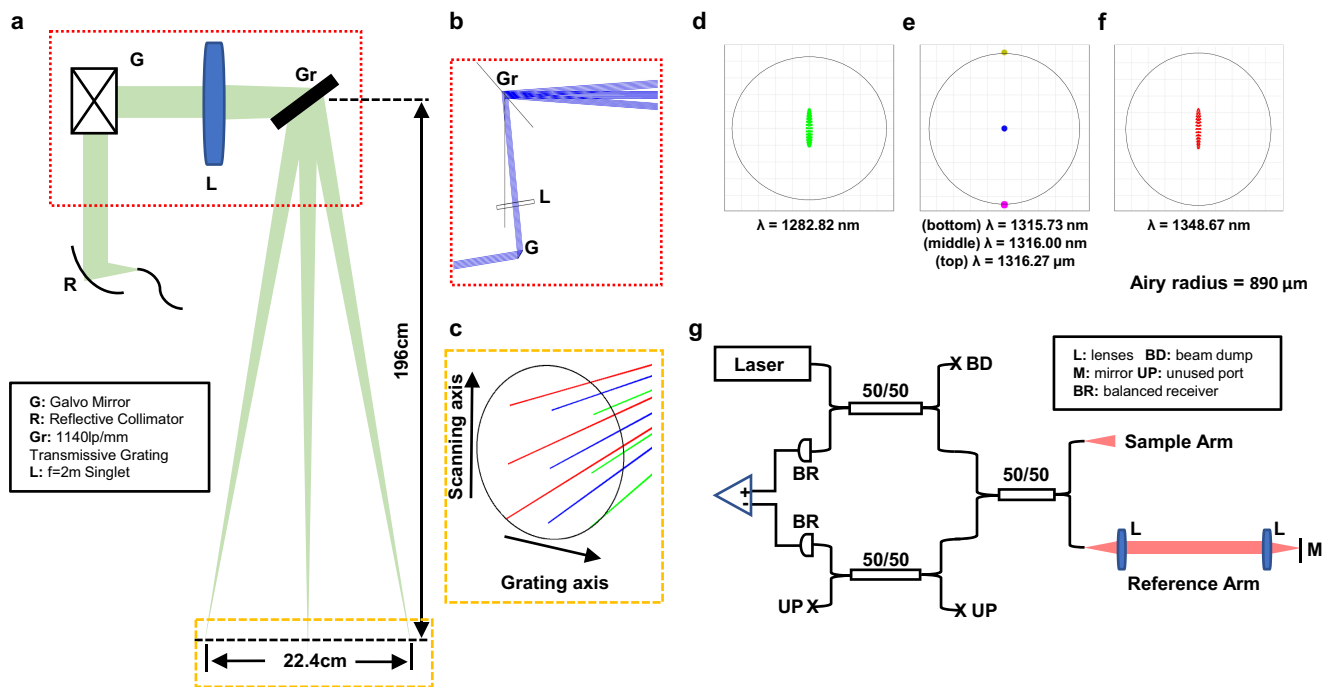


Fig. 1 Optical and system design of the real-time time-frequency multiplexed FMCW LIDAR system. **a** Schematic of the sample arm optical design and **b, c** corresponding zoomed-in Zemax design; **d-f** Spot diagrams at the imaging plane of the **d** first, **e** central, and **f** last wavelengths, along with **e** two wavelengths that have centroids of spots located adjacent to the central wavelength with a separation distance of the Airy radius at the focus; **g** Schematic of the overall system design.

three factors: the coherence length or instantaneous linewidth of the swept laser, the maximum sampling speed of the digitizer, and the bandwidth of the photodetector. In our current setup, the maximum imaging range without significant sensitivity roll-off was approximately 32 cm, limited by both the sampling speed of the digitization card (800MS/s) and the bandwidth of the photodetector (400 MHz).

Signal processing. With a grating used for fast spectral scanning, the detected interferogram during a single sweep contains the signals from reflectors at different lateral positions along the horizontal axis. To retrieve the depth information of reflectors, instead of Fourier transforming the entire interferogram, a short-time Fourier transform (STFT) was applied (Fig. 2a). The spectral window size of the STFT determines the tradeoff between the angular/lateral resolution and axial resolution. A larger spectral window corresponds to a larger bandwidth, which leads to better axial resolution or localization accuracy, but fewer total number of windows, which leads to lower effective lateral resolution along the grating axis. Here, the optimal spectral window size was determined based on the lateral resolution of the system. As shown in Fig. 1e, if point spread functions of two adjacent wavelengths are unresolvable (i.e., the centroid of the spot of one wavelength is within the Airy radius of the other wavelength), the detected signals from these two wavelengths were treated as arising effectively from the same position, and were therefore analyzed within the same spectral window. As such, we determined the optimal spectral window size of 1.56 cm^{-1} in wavenumber or 0.27 nm in wavelength at $\sim 1316\text{ nm}$ for our design, which corresponded to about 200 samples per window. The effective lateral resolution of the system along the grating axis was then determined by the sum of point-spread functions (PSFs) of all the wavelengths within the same spectral window, which is equivalent to the convolution of the PSF of single wavelength and the STFT window. Thus, the lateral resolution along the grating

axis was determined to be $1240\text{ }\mu\text{m}$ in this design (see Supplementary Fig. 1), while the lateral resolution along the galvanometer axis was still $890\text{ }\mu\text{m}$, determined solely by the imaging optics as in conventional optical imaging.

The truncated signal from each spectral window (Fig. 2a) was then zero-padded to 5000 samples before taking the Fourier transform (FT). Here, zero-padding enabled more accurate, sub-pixel peak localization. The depth of the dominant reflector was then localized if the peak intensity after taking the FT was above a predefined threshold (Fig. 2b), detailed in the Methods section), otherwise that pixel was considered as background with no detected reflector and the depth value was assigned to not available (N/A). To achieve Nyquist lateral sampling, two adjacent spectral windows were overlapped by one half the window size (Fig. 2a), which was 100 samples or 0.78 cm^{-1} in wavenumber. Therefore, a total of 475 spectral windows were applied in each sweep/A-scan, which means 475 depth measurements (238 independent depth measurements) were obtained within a single sweep time of $62.7\text{ }\mu\text{s}$. Finally, the depth map was acquired by scanning the beam in the slow axis using the galvanometer mirror, and performing the same STFT and peak localization analysis for each laser sweep.

Localization precision & accuracy characterization. Our time-frequency multiplexed FMCW imaging technique is analogous to stochastic optical reconstruction microscopy (STORM) in the sense that both techniques are localization-based methods with corresponding sparsity requirements. STORM localizes the centroids of a subset of fluorophores that are activated at a given time with a typical precision down to tens of nanometers to achieve super-resolution imaging beyond the diffraction limit²⁷. Similarly, our technique localizes the depth of an object assuming it has a dominant reflector (most likely the surface reflector) and achieves localization precision and accuracy better than the purely optical imaging resolution.

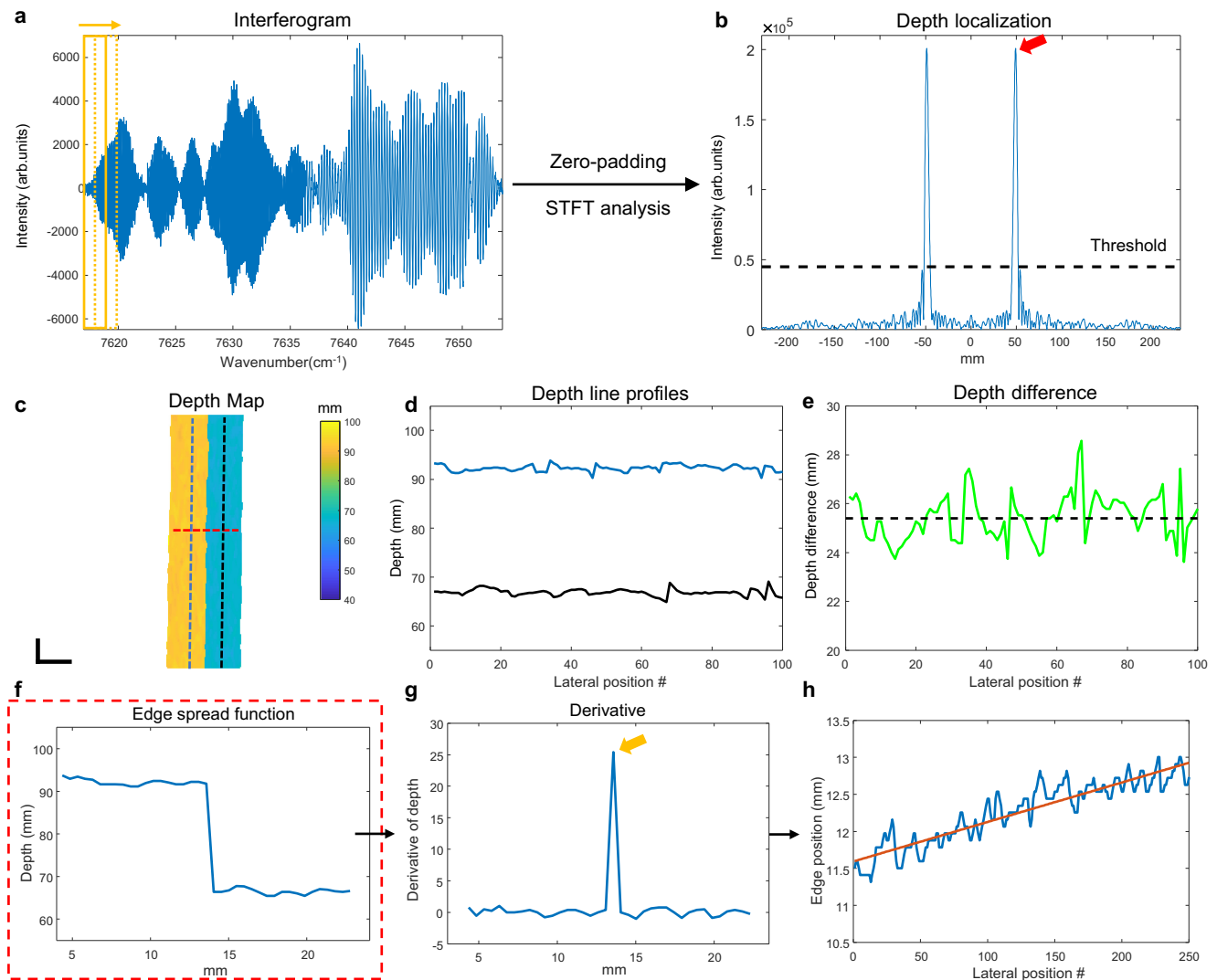


Fig. 2 Signal processing and system performance characterization of the time-frequency multiplexed FMCW LiDAR system. **a** Short-time Fourier Transform (STFT) analysis to retrieve the depths of reflectors along the grating axis and **b** depth localization from the signal after FT and. **c** Depth map of two staggered metal base plates separated by 25.4 mm, scale bar: 1 cm. **d, e** The “scanning spot” axial localization precision and accuracy characterization: **d** depth profiles along two lines of the front (black line in **c**) and back metal plates (blue line in **c**) and **e** their depth differences. **f, h** The lateral localization precision characterization: **f** the edge spread function of the depth profile along the red line in **c** and **g** the edge localization from its calculated derivative function, and **h** the residual localization error measured at 250 lateral positions.

In the axial direction, we characterized both the axial localization accuracy and precision of the system. Here, axial localization precision refers to the uncertainty or repeatability of our axial localization, while axial localization accuracy refers to how close our depth measurement was to the ground truth depth.

Same spot axial localization precision—mirror and diffuse scattering sample. To quantify the axial localization precision for an ideal reflecting sample, we first imaged a gold mirror behind neutral density filters with various optical densities (ODs), which is a standard experiment in OCT to characterize axial resolution and sensitivity. We took data from 400 repeated laser sweeps on the mirror sample without any vertical galvanometer scanning, and calculated the SD of the retrieved depths at the same location along the horizontal grating scan direction (later referred to as the “same spot” axial localization precision). We performed these measurements at three different input power or SNR levels. Assuming the gold mirror is a perfect single reflector, the normalized interferogram $S(\mathbf{k})$ can be modeled using the following

equation,

$$S(\mathbf{k}) = A \cos(2k\Delta z + \varphi) + \text{Gauss}(0, \sigma) \quad (1)$$

where A and φ are amplitude and phase of the interference fringe, and Δz is the depth of the reflector. Defining a shot noise limited FMCW system as a hypothetical system whose dominant source of noise is shot noise arising from reference light power²⁸, in the limit of a large number of photons the noise is approximately normally distributed, $\text{Gauss}(0, \sigma)$, with an SD of σ . Based on this model, the minimum theoretical localization uncertainty of Δz has previously been derived²⁹, which in practice can be achieved using the aforementioned Fourier-domain zero-padding approach²⁹. The SD of the Δz localization, δz , can be estimated using the following equation²⁹,

$$\delta z \approx (1.6 \times \text{SNR} \times 2\Delta k \sqrt{N_s})^{-1}, \quad (2)$$

where Δk is the total bandwidth in wavenumber, and N_s is the total number of spectral sampling points. In our system, the number of sampling points, N_s , in each STFT window was 200,

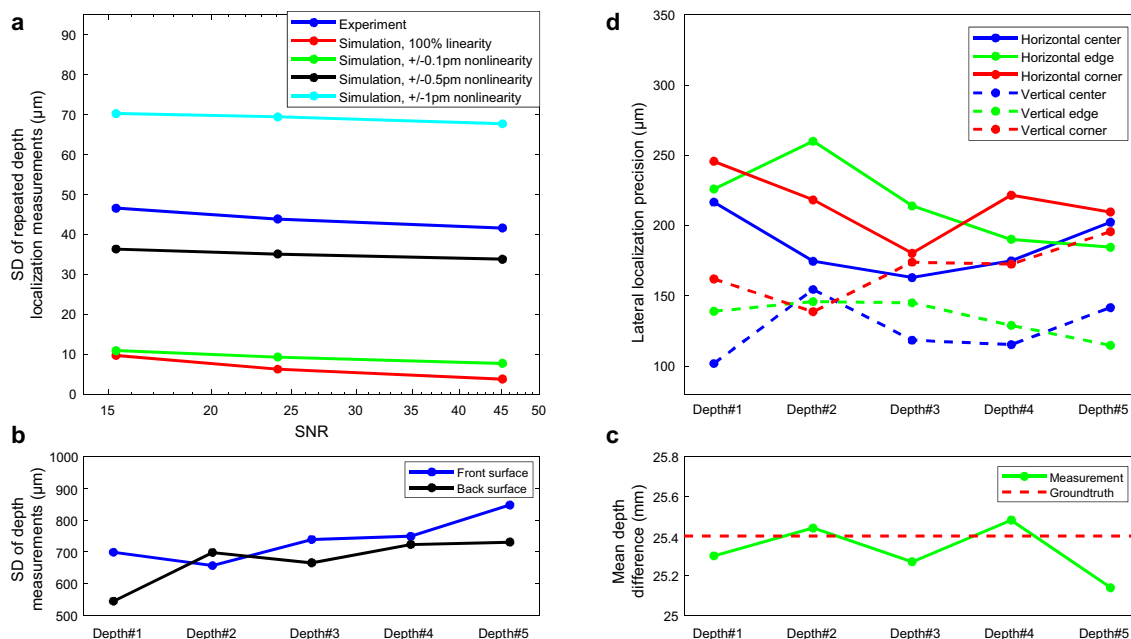


Fig. 3 Results of system localization precision and accuracy characterization. **a** Measured axial localization precision calculated from the standard deviation (SD) of repeated depth measurements at the “same spot” in the grating scan direction, using an ideal mirror sample. Also plotted are the theoretical axial localization precisions with various wavenumber nonlinearity coefficients (0, ±0.1, ±0.5 and ±1 pm) at three different signal-to-noise ratios (SNRs). Measured axial localization **b** precision and **c** accuracy calculated from the SD of depth measurements from multiple “scanning spots” along two lines in the galvanometer scan direction using a diffuse scattering sample (two staggered anodized aluminum plates). Plotted are **b** the SD of the depths of the front and back surfaces of the plate and **c** the mean depth difference at five different depths (-4, 10, 16, 22, and 28 cm). **d** Horizontal and vertical localization precisions at three different depth locations (-4, 10, 16, 22, and 28 cm) and three different lateral positions (center: -[0,0] cm; edge: -[10,0] cm; corner: -[10,10] cm) within the measurement field-of-view.

and the bandwidth of each window, Δk , was 1.56 cm^{-1} . Here, the SNR of the detected interferogram is defined as²⁹,

$$\text{SNR} = \frac{A}{\sqrt{2}\sigma} \tag{3}$$

Using this equation, we calculated the SNRs of our detected interferograms, and a plot of the SDs of the retrieved depths at three different SNR levels is shown in the dark blue line in Fig. 3a. Assuming 100% sweeping linearity, the theoretical SDs of depth localization at the same SNR levels as the experimental data are calculated using Eq. 2 and plotted in red line in Fig. 3a. We then compared our experimental results with the theoretical predicted axial localization precisions at these corresponding SNR levels. As expected, the localization precision increased as the SNR of the detected signal increased (experiment: from 46.5 μm to 41.6 μm ; simulation: 9.69 μm to 3.79 μm). However, the measured SDs from our experiment were more than 4× worse than the theoretical SDs.

The model of Eq. 2 assumes 100% laser sweeping linearity, such that adjacent spectral sampling points are evenly separated in space. To also include the effect of sweeping nonlinearity, we extend the model to include sweep nonlinearity using the following equation

$$S(\mathbf{k}) = \text{Acos}(2(\mathbf{k} + \text{Gauss}(0, \sigma_k))\Delta z + \varphi) + \text{Gauss}(0, \sigma) \tag{4}$$

Here, $\text{Gauss}(0, \sigma_k)$ is the gaussian wavenumber nonlinearity noise with a SD of σ_k . Using this extension to the model, we simulated $S(\mathbf{k})$ with Δz the same as the experiment data, and various σ_k ranging from 0.1 pm ($5.8 \times 10^{-4} \text{ cm}^{-1}$) to 1 pm ($5.8 \times 10^{-3} \text{ cm}^{-1}$) at the same SNR levels and calculated the SD of depth localization. The results are plotted in green, black and cyan lines in Fig. 3a. Our experiment results are closest to the simulation results with ±0.5 pm nonlinearity (black line), which is

also the nonlinearity specification provided by the laser manufacturer³⁰. Thus, in our system, it is clear that the sweep nonlinearity played a more significant role in determining the same spot axial localization precision in this application.

On the other hand, the OCT axial resolution, defined as the coherence length of the laser over the wavelength sweep range per acquisition, is calculated using the below equation,

$$l_c = \frac{2 \ln 2}{\pi} \frac{\lambda_0^2}{\Delta \lambda} \tag{5}$$

where λ_0 and $\Delta \lambda$ are the central wavelength and the bandwidth of the source³¹. In our system, the bandwidth of each STFT window was 1.56 cm^{-1} or 0.27 nm at 1316 nm, and the corresponding theoretical OCT axial resolution (i.e., coherence length associated with that bandwidth) was 2.82 mm. Meanwhile, our measured localization precisions were 41.6–46.5 μm , indicating that our same spot localization precision for an ideal mirror sample was >60× better than the theoretical axial resolution.

We note that for a grating-scanned system with non-telecentric scanning, a mirror or other specularly dominant reflector is useful for comparison with theory, but the results for localization accuracy and precision may differ from real-world diffusely scattering samples since a mirror artificially enforces an exact back-scattering requirement. Therefore, for the remainder of our localization accuracy and precision measurements, in order to depict real-world performance, diffusely scattering samples were used.

For our repeated same spot measurement of the diffusely scattering anodized aluminum sample, the SD of depth localization at a single lateral position on the sample was 64.2 μm . While we did not have means to accurately measure the SNR of the signal from this sample, this result was not significantly worse than the mirror results for which the SNRs were known as

depicted in Fig. 3a. (41.6–46.5 μm). We also measured the full width at half maximum (FWHM) of the peak in the FFT signal for each STFT window, and the averaged FWHM measured from a total of 238 STFT windows across the whole bandwidth was found to be 3.43 mm, which is close to our theoretical axial resolution, 2.82 mm, calculated using the coherence length equation (see Supplement S4 for details).

Scanning spot axial localization precision & accuracy—diffuse scattering sample. To characterize any additional contributions to axial localization uncertainty arising from lateral scanning, we performed “scanning spot” measurements using two staggered metal base plates separated by 25.4 mm in depth (Fig. 2c), detailed in the “Methods” section). Our measurements results characterizing the scanning spot axial localization precision and accuracy for the anodized aluminum sample are depicted in Fig. 3b, c, in which the axial localization accuracy results measured at five different depths (~4, 10, 16, 22, and 28 cm) using the staggered metal plate sample are shown. The SDs of depth localization obtained from 100 different positions at the front surface and the back surface along two lines (Fig. 2c) are plotted in Fig. 3b, and the mean measured depth differences at five different depths were 25.30 mm, 25.44 mm, 25.27 mm, 25.48 mm, and 25.14 mm, which were all close to the ground truth, 25.40 mm (Fig. 3c). Interestingly, the SDs of the scanning spot depth localization measurements across the metal sample (~500–800 μm) were ~7–11 \times worse than the SD of the same spot depth localization at a single lateral position in the same metal sample (64.2 μm). Since the surface roughness of these professionally machined surfaces is expected to be substantially less than 0.5 mm, this difference is likely due to independent realizations of speckle as a function of lateral position arising from the distribution of sub-resolution reflectors in the diffusely scattering sample, including those below the surface. Nevertheless, even for this real-world sample, the measured axial localization precision still exceeded the theoretical OCT axial resolution, given the laser bandwidth used to obtain the depth measurement, by ~4 \times . We note that scanning spot precision and accuracy are clearly sample dependent. The values are expected to be closer to the same spot precision when the sample is more like a specular reflector (i.e., a dominant single reflector with minimal surface roughness).

Lateral localization precision—diffuse scattering sample. Finally, we characterized the lateral localization precision of our system by imaging the same staggered metal plates and quantifying the uncertainty of the edge localization (detailed in the “Methods” section). The horizontal and vertical localization precisions measured using the same staggered metal piece at five depths (~4, 10, 16, 22, and 28 cm) and three different lateral positions (center: ~[0, 0] cm; edge: ~[+10, 0] cm; corner: [+10, +10] cm) are shown in Fig. 3d. Overall, the localization precisions in both directions were uniform across the imaging depth and lateral FOV. The mean and SD of vertical localization precision was 143.2 μm and 24.8 μm , while the mean and SD of the horizontal localization precision was 205.4 μm and 26.7 μm . It was expected that the vertical localization precision would be better than the horizontal localization precision, as the vertical resolution (~890 μm) of our imaging system is better than the horizontal resolution (~1240 μm) due to STFT analysis. Nevertheless, this result demonstrates that our system localized the reflector depth variation laterally better than the optical resolution of the system.

3D imaging results on everyday samples. We performed 3D imaging on multiple static samples and a living human hand.

First, to demonstrate the long axial imaging range of our system, we imaged two ceramic coffee cups (Fig. 4d), which were axially separated by >9 cm. 1000 scans across a vertical FOV of 15 cm were acquired, which corresponds to a 3D imaging frame rate of 15.94 Hz. The processed depth map with 475 \times 1000 pixels (spanning 22.4 \times 15 cm) and the corresponding 3D rendering of cups are shown in Fig. 4a, b. In Fig. 4c, we plot the cross-section depth profile along the black line in Fig. 4a); the contour of the cup can be clearly observed.

To demonstrate that this technology can image objects with relatively weak surface reflections, we first imaged a synthetic rubber mannequin head (Fig. 4h). Similar to the coffee cup imaging, 1000 scans across a vertical FOV of 15 cm were acquired, corresponding to the same 3D imaging frame rate of 15.94 Hz. Due to relatively weak scattering signal from the sample, the intensity thresholding-based depth localization approach was not sufficient to localize the depth of every reflector within the sample. Additionally, when a lower threshold value was applied, more background stripe noise was introduced due to imperfect removal of invalid points during the transitions between subintervals of a laser sweep³² (Supplement Fig. 2a). Therefore, we applied a gradient-based background noise removal algorithm along with a 3 \times 3 median filter to create the final depth map and 3D volume rendering (see Supplement Fig. 2). The representative depth map and the corresponding volume rendering of the head are shown in Fig. 4e, f. In Fig. 4g, we plot the cross-section depth profile along the black line in Fig. 4e. The contours of the forehead, nose, upper and lower lip can clearly be resolved.

Finally, we demonstrate that our technology can not only achieve video-rate 3D ranging that allows us to image moving objects, but also be applied for in vivo imaging. Here, we imaged a hand adjacent to a metal stage and actively making a fist. 480 scans (including 80 scans for galvanometer flyback) across a vertical FOV of 16 cm were acquired, which corresponds to a frame rate of 33.2 Hz. The final depth maps with 475 \times 400 pixels (spanning 22.4 \times 16 cm) and the corresponding 3D renderings of the hand at different times are shown in Fig. 4i, j. For the depth maps in Fig. 4i, the same noise removal method discussed for the face in 4e, f was applied. For the volume rendering in Fig. 4j, to further remove the background stripe noise, an 8 \times 8 median filter was used. A ~2 s video (67 frames) of the volume rendering played in 0.5 \times speed is shown in Supplement Movie 1. Although human skin is a relatively weakly scattering sample, the depth map of skin is still retrieved with high axial localization accuracy.

Discussion

Our time-frequency multiplexed FMCW system achieves high-speed high-precision 3D imaging by using a broadband swept source with narrow instantaneous linewidth and a diffraction grating for spectrally encoded fast axis scanning. By applying a compressed sampling approach using an optimized window size and zero padding, 238 independent depth measurements along the grating axis were obtained within a single sweep time. Although each window had a narrow bandwidth of 1.56 cm^{-1} , we demonstrated on both mirror and metal samples that the axial localization accuracy and precision were significantly better than the theoretical resolution, which was nearly 3 mm. 3D imaging of multiple static samples and video-rate imaging of a moving human hand demonstrate the great potential of this technology in a wide range of potential applications in the fields of robotics navigation, virtual reality and 3D printing.

Although FMCW LiDAR combined with a diffraction grating for spectrally encoded scanning has previously been reported²⁵, our work provides a rational basis for optimizing system

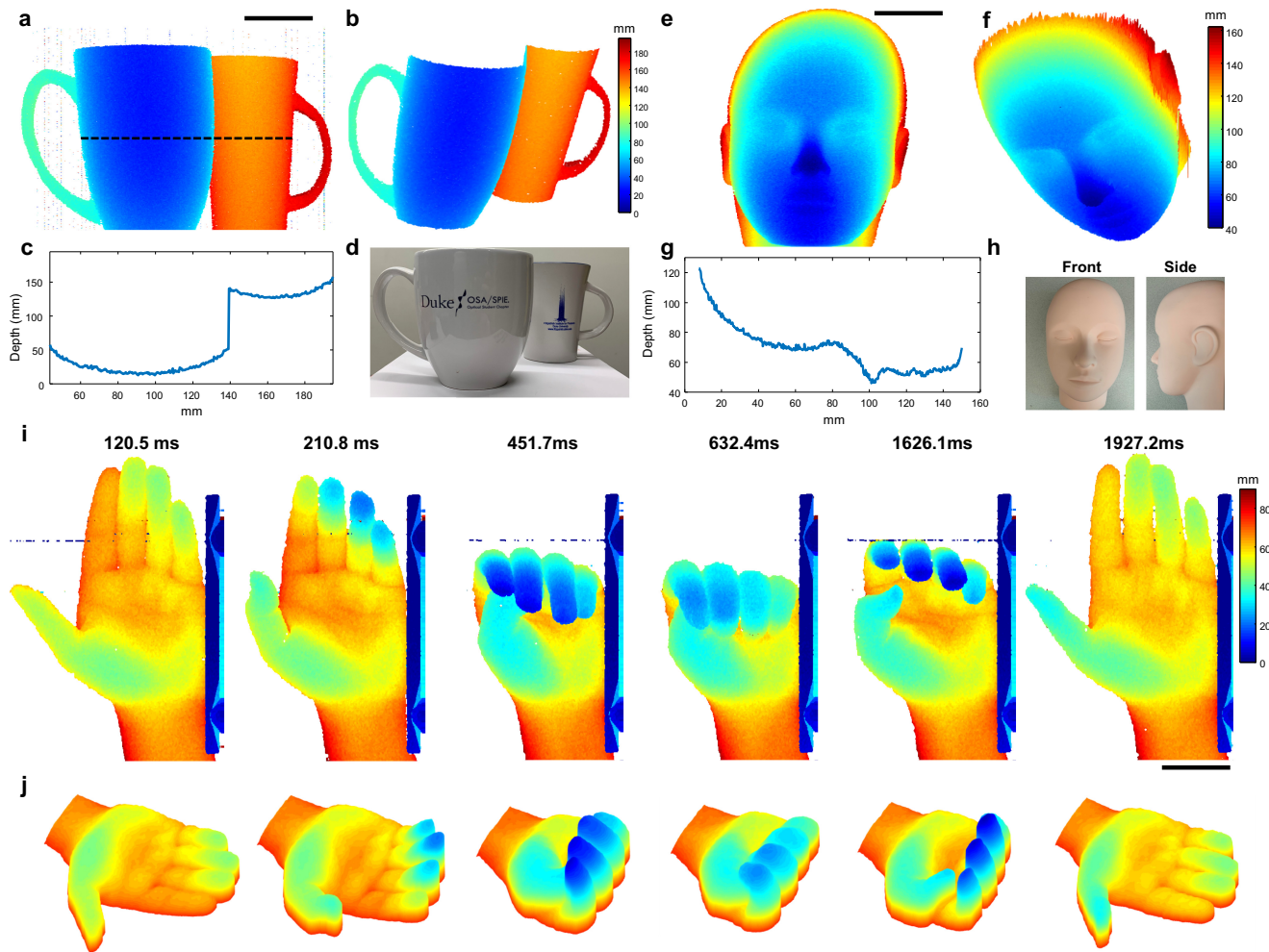


Fig. 4 Video-rate 3D imaging results of real-world objects. **a–d** Imaging results of two ceramic coffee cups axially separated by >9 cm, imaged with 475×1000 depth pixels at 16 Hz: **a** depth map and **b** 3D surface rendering of the cups; **c** cross-section depth profile along the black line in **(a)**; **d** photo of the cups. **e–h** Imaging results of a mannequin head, imaged with 475×1000 depth pixels at 16 Hz: **e** depth map and **f** 3D surface rendering of the mannequin head; **g** cross-section depth profile along the black line in **e**; **h** Front and side views of the mannequin head. **i, j** Imaging results of a human hand adjacent to a metal stage and actively making a fist, imaged with 475×400 depth pixels at 33.2 Hz: **i** depth maps and **j** 3D surface renderings of the hand while flexing; shown are 6 individual frames from a 2 s video acquired with a frame rate of 33.2 Hz. See Supplement Movie 1 for the complete video. Scale bar: 5 cm.

performance based on advancing understanding of the interplay of lateral resolution and depth localization precision and accuracy. First, we demonstrate that the size of each STFT spectral window should be carefully designed based on the lateral resolution of the system. If point spread functions (PSFs) of two adjacent wavelengths are unresolvable (i.e. the centroid of the spot of one wavelength is within the Airy radius of the other wavelength), the detected signals from these two wavelengths can then be treated as arising effectively from the same position, and should be therefore analyzed within the same spectral window during STFT. The optimal selection of the STFT spectral window size minimizes the reduction of lateral resolution along the grating axis, while still maintaining high depth localization precision. In addition, it enables a nearly isotropic lateral resolution ($\sim 890 \mu\text{m}$ along the scanning axis and $\sim 1240 \mu\text{m}$ along the grating axis), which is highly desired for a 3D ranging system. Secondly, we showed that, although there were only 200 spectral points within each window, by zero-padding the signal before performing Fourier transform and peak localization, we were able to achieve depth localization precision >60x better than the

theoretical depth resolution. In addition, we further demonstrated and validated a theoretical localization precision model from the fundamental signal perspective, with the model incorporating key parameters of a FMCW LiDAR system, such as SNR, laser bandwidth, total number of spectral points and sweep nonlinearity. Finally, with the enhanced system sensitivity and localization precision combined with large data-throughput (475×500 depth measurements at a frame rate of 33.2 Hz), our work demonstrated video-rate high-precision 3D live human imaging, which, to our knowledge, has not been demonstrated in any prior FMCW LiDAR work.

One of the potential advantages of the proposed FMCW LiDAR system over conventional ToF-based LiDAR systems is the improved depth precision. There are two major types of ToF LiDAR, pulsed ToF (also called direct ToF) and amplitude-modulated continuous wave (AMCW) LiDAR (also called indirect ToF). To achieve high depth precision, nanosecond pulses and high-speed photodetectors with tens-of-picosecond sampling speeds, such as a single photon avalanche diodes (SPADs) or SPAD arrays, are typically used. However, recently

reported direct ToF LiDAR systems have at best millimeter or centimeter-scale depth localization precisions³³. Submillimeter depth localization precision remains difficult to achieve with the limited electronic detection bandwidth of photodetectors. AMCW, or indirect ToF, determines the distance to objects by emitting continuous intensity-modulated light and measuring the returned signal multiple times to compute the phase delay. By modulating the light at tens or hundreds of MHz, AMCW LiDAR can achieve meter-scale imaging ranges but also only millimeter or centimeter-scale depth localization precisions³³, similar to pulsed ToF LiDAR. FMCW LiDAR is fundamentally different from ToF LiDAR. Instead of modulating the intensity of the emitted light at several GHz in most, FMCW LiDAR directly modulates the optical frequency of the emitting light at hundreds of GHz or even THz, as demonstrated in this paper, which inherently leads to higher ranging precision.

In addition, FMCW LiDAR can potentially provide higher sensitivity than ToF LiDAR in general. As incoherent detection methods, AMCW or pulsed LiDAR can be more easily affected by ambient or stray light, which can lead to reduced system sensitivity and/or inability to operate in daylight. More importantly, in FMCW LiDAR, interfering the weak light reflected from the sample with higher intensity reference arm light enables measurement sensitivity to be limited by quantum effects instead of other sources of noise, such as thermal noise of the detector. Therefore, the coherent heterodyne detection with sufficient reference arm power allows high sensitivity approaching the shot noise limit to be achieved with simpler and cheaper (i.e. uncooled and non-avalanche) detectors, and thus potentially achieve higher sensitivity.

Also available for room-scale high-resolution 3D imaging, structured light sensors are a robust 3D imaging technology that also achieves submillimeter depth localization accuracy using high-end projectors and cameras. Structure light sensors are a mature technology which can readily achieve video-rate imaging with high lateral resolution at low cost. However, compared to our proposed FMCW LiDAR system, structured light camera has several major disadvantages, including the inherent tradeoff between the maximum imaging range and the depth resolution (similar to AMCW LiDAR), high sensitivity to ambient light and difficulty in measuring inclined objects or surfaces that create shadows³⁴.

One major limitation of our current imaging system is the relatively short imaging depth range of 32 cm, which is currently limited by the bandwidth of our available photodetector and digitizer. Using a commercially available higher speed digitizer, 10GS/s, along with a similarly available photodetector with sufficient bandwidth (2.5 GHz), the imaging range of our system could be further extended to about 2 m. An increase of sampling rate would also lead to more sampling points per STFT window, improving the localization precision as predicted by Eq. (3). To further increase the imaging range without upgrading the digitizer and the photodetector, one approach would be to use a swept source laser with a narrower total bandwidth with a tradeoff of the depth localization accuracy, and another approach is to reduce sweep rate of the laser with a tradeoff of the frame rate.

Another limitation of our current system is the limited lateral FOV along the horizontal axis. The horizontal angular FOV is fundamentally determined by the bandwidth of the source and the groove density of the grating. With a 65 nm bandwidth centered at 1316 nm and a 1145 grooves/mm grating, an angular FOV of 7.1° was achieved. To increase the angular FOV, a source with a larger bandwidth or a grating with a larger groove density could be used. Or, without changing the angular FOV, the lateral FOV could also be extended by simply increasing the working distance, although an imaging lens with a longer focal length or even a collimated beam needs to be used to extend the axial

location of the focal plane. A telescope could also be added after the grating to expand the angular FOV.

Although the imaging speed of our system is not currently limited by the bandwidth of the galvanometer scanner, 2D solid-state beam steering is still desired in LiDAR technologies due to its advantage of high steering speed, repeatability and stability. In ToF LiDAR, non-scanning imaging can typically be achieved by using either an array of sensors (e.g., SPAD array) or optical phased arrays. In our current prototype, solid-state scanning is only achieved along the grating axis, while the other axis still relies on mechanical scanning. However, 2D solid-state spectral scanning can potentially be achieved by using cascaded gratings³⁵, array waveguide grating³⁶, and virtually imaged phased array³⁷.

A total of 238 independent depth measurements were obtained within a single sweep with current setup. To increase the number of independent measurements per sweep without changing the laser and grating, a narrower STFT window needs to be used, which means a more tightly focused beam with better lateral resolution is needed. However, this will potentially lead to worse axial localization accuracy and precision, as explained in Eq. (3), as well as shorter depth of focus. Therefore, the numerical aperture (NA) of the imaging beam determines the tradeoff between the total number of resolvable measurements along the grating axis and the axial localization precision and depth of focus. The optimal choice of the NA depends on the applications and will be further investigated in the future studies.

Our measured same spot axial localization precision of the system was more than 4× larger than the theoretical localization precision at the same SNR level, and based on our simulation studies, the main source of error is likely to be the sweep non-linearity, which is about ±0.5 pm for our current swept laser. To further improve the system precision, besides using a swept laser with higher sweep linearity, another possible approach is to perform a more accurate characterization and correction of sweep nonlinearity. This can potentially be achieved by sampling and monitoring the k-clock signal using another independent Mach-Zehnder interferometer clock box, which is a standard technique used in swept-source OCT.

Our measured same spot axial localization precision on both mirror and machined metal samples was also about an order of magnitude better than the measured scanning spot axial localization precision on the metal sample. Here, the same spot axial localization precision can be considered as the system-limited axial localization precision, since this value only depends on the SNR of the detected signal and sweep linearity of the source as shown above, while the scanning spot localization precision can be considered as the sample-limited axial localization precision, as it includes any additional contributions to axial localization uncertainty arising from sample roughness or other deviations from the single reflector assumptions. It is notable that the sample-limited axial localization precision on the mirror sample could not be measured, since the optical system was not telecentric and thus only a very small central region of the mirror satisfied the exact backscattering requirement. The difference between system-limited and sample-limited localization precisions on the metal sample is likely due to the effects of speckle. Since the adjacent wavelengths in each STFT window are not completely overlapped, and the metal is not a single specular reflector, different wavelengths interact with different sub-resolution reflectors, leading to speckle. With a narrow bandwidth of 1.56 cm⁻¹, the effect of speckle is even more significant, as also observed in a previous grating-based scanning microscopy system³⁸. To reduce this effect, besides using a broader bandwidth source and a larger STFT window, methods such as spatial or angular compounding could also be considered^{39,40}.

In conclusion, we demonstrated a time-frequency multiplexed FMCW ranging system that combines grating-based spectrally encoded fast scanning and optimal STFT analysis for depth retrieval. The system can perform video-rate high-precision 3D imaging with an imaging range of 32 cm, and potentially be used in many emerging industrial, automotive, and biomedical fields.

Methods

Akinetic all-semiconductor programmable swept source. An akinetic all-semiconductor programmable swept laser source (Insight Photonics Solutions; Lafayette, CO) centered at 1316 nm with a 65.85 nm bandwidth was used. The source has an output power of ~70 mW and a nearly flat power spectrum across the entire bandwidth. The source also has an instantaneous coherence length of >1 m and a linearity $\leq \pm 0.5$ pm root mean square without the need for an external k-clock³⁰. The sweep rate of the laser can be adjusted from 10 kHz to 200 kHz, and for this application, we set the sweep rate of the laser at 15.94 kHz.

Time-frequency multiplexed FMCW LiDAR optical design. A 4 mm diameter collimated beam was created by a reflective collimator (Thorlabs; Newton, NJ), and then focused by a 2 m focal length plano-convex lens (Thorlabs; Newton, NJ) (Fig. 1a). A galvanometer mirror (Thorlabs; Newton, NJ) was inserted before the imaging lens to accomplish beam scanning along the slow (vertical) axis, while a 1145 grooves/mm volume phase holographic transmissive grating (Wasatch Photonics; Logan, UT) was placed immediately after the lens to achieve spectrally encoded scanning along the fast (horizontal) axis. The grating was positioned with an incident angle of $\sim 48^\circ$ to maximize diffraction efficiency, and the input beam power after the grating was 15.2 mW. With the total sweep bandwidth of the input source of 65.85 nm, the angular FOV along the horizontal axis was 7.1° . With a working distance (from the grating to the focal plane) of 196 cm, the system thus achieved a horizontal FOV of 22.4 cm and diffraction limited performance with a lateral resolution of 890 μm at the focus along the galvanometer scanning axis (Fig. 1d–f).

Predefined threshold for depth localization. Here, the threshold to determine the peak localization of each processed signal was defined using the following method. First, a baseline measurement without any objects in the imaging FOV was taken, and the same zero-padding and STFT analysis was performed on the measurement. We then calculated the mean, μ_I , and standard deviation, σ_I , of the peak intensity across the whole FOV. We used $2 * \sigma_I$ above the mean baseline intensity, μ_I , as our intensity threshold for peak localization when imaging real-world objects. Since the sample arm illumination power and reference arm power remained constant during those measurements, we used the same threshold value. In Supplement Sec. 3, we also explored the depth map results with different threshold values to illustrate that this predefined threshold is a reasonable value for the depth localization of our system.

Scanning spot axial localization precision & accuracy. To characterize scanning spot axial localization precision and accuracy, we imaged two staggered metal base plates separated by 25.4 mm in depth (Fig. 2c). We measured the depth profiles (Fig. 2d) along two lines in the galvanometer scan direction (blue and black lines in Fig. 2c) of the front and back metal plates. We defined the scanning spot axial localization precision as the SD of the depth localization from multiple laterally displaced locations along the galvanometer scan direction line, and the scanning spot axial localization accuracy as their depth difference (Fig. 2e), to be compared to the ground truth depth difference of 25.4 mm (red line in Fig. 2e). We repeated this measurement at five different axial positions (~4, 10, 16, 22, and 28 cm).

Lateral localization precision. We characterized the lateral localization precision of our system by imaging the same staggered metal plates and quantifying the uncertainty of the edge localization. To measure the horizontal localization precision, we aligned the edge of metal plates perpendicular to the grating/horizontal axis, and obtained the depth map using the same STFT processing method described above, except that for characterization purposes, we oversampled the depth map by having two adjacent STFT windows separated by 10 samples or 0.08 cm^{-1} in wavenumber. We plotted the resulting edge response function (Fig. 2f) along the horizontal axis (red line in Fig. 2c) and obtained the depth range measurement as the peak of its derivative (Fig. 2g). We repeated this measurement at 250 consecutive lateral positions along the vertical axis. Finally, we fit the peak location profile with a line to remove the residual tilt due to imperfect alignment of metal plates, and calculated the residual standard deviation (Fig. 2h), to arrive at the horizontal localization precision. Using the same approach, we measured the vertical localization precision by imaging the same metal base plates rotated by 90 degrees. We placed the base plates at three different lateral positions (center: $\sim [0, 0]$ cm; edge: $\sim [+10, 0]$ cm; corner: $[+10, +10]$ cm) and five different axial positions (~4, 10, 16, 22, and 28 cm) to quantify the horizontal and vertical lateral localization precision over the entire 3D imaging space.

Data availability

The raw interferogram data have been deposited at: <https://doi.org/10.6084/m9.figshare.19144388>. Any other data that support the findings of this study are available from the corresponding author upon reasonable request.

Code availability

Code used in generating 3D depth map from raw interferogram data is available at: <https://github.com/ruobingqian/time-frequency-fmcw-lidar>.

Received: 12 October 2020; Accepted: 25 February 2022;

Published online: 29 March 2022

References

- Huang, D. et al. Optical coherence tomography. *Science* **254**, 1178–1181 (1991).
- Hee, M. R. et al. Optical coherence tomography of the human retina. *Arch. Ophthalmol.* **113**, 325–332 (1995).
- Wieser, W., Biedermann, B. R., Klein, T., Eigenwillig, C. M. & Huber, R. Multi-megahertz OCT: high quality 3D imaging at 20 million A-scans and 4.5 Gvoxels per second. *Opt. Express* **18**, 14685–14704 (2010).
- Riemensberger, J. et al. Massively parallel coherent laser ranging using a soliton microcomb. *Nature* **581**, 164–170 (2020).
- Dieckmann, A. FMCW-LIDAR with tunable twin-guide laser diode. *Electron. Lett.* **30**, 308–309 (1994).
- Huang, M. C. Y., Zhou, Y. & Chang-Hasnain, C. J. A surface-emitting laser incorporating a high-index-contrast subwavelength grating. *Nat. Photonics* **1**, 119–122 (2007).
- Potsaid, B. et al. in *Proceeding SPIE BiOS 8213* (International Society for Optics and Photonics, 2012).
- Wang, Z. et al. Cubic meter volume optical coherence tomography. *Optica* **3**, 1496–1503 (2016).
- Moon, S. & Choi, E. S. VCSEL-based swept source for low-cost optical coherence tomography. *Biomed. Opt. Express* **8**, 1110–1121 (2017).
- Qiao, P., Cook, K. T., Li, K. & Chang-Hasnain, C. J. Wavelength-swept VCSELs. *IEEE J. Sel. Top. Quantum Electron.* **23**, 1–16 (2017).
- Hariyama, T., Sandborn, P. A. M., Watanabe, M. & Wu, M. C. High-accuracy range-sensing system based on FMCW using low-cost VCSEL. *Opt. Express* **26**, 9285–9297 (2018).
- Huber, R., Wojtkowski, M. & Fujimoto, J. Fourier domain mode locking (FDML): a new laser operating regime and applications for optical coherence tomography. *Opt. Express* **14**, 3225–3237 (2006).
- Xu, J., Zhang, C., Xu, J., Wong, K. & Tsia, K. Megahertz all-optical swept-source optical coherence tomography based on broadband amplified optical time-stretch. *Opt. Lett.* **39**, 622–625 (2014).
- Siddiqui, M. et al. High-speed optical coherence tomography by circular interferometric ranging. *Nat. Photonics* **12**, 111–116 (2018).
- Dilazaro, T. & Nehmetallah, G. Large-volume, low-cost, high-precision FMCW tomography using stitched DFBs. *Opt. Express* **26**, 2891–2904 (2018).
- Zhang, X., Pouls, J. & Wu, M. C. Laser frequency sweep linearization by iterative learning pre-distortion for FMCW LiDAR. *Opt. Express* **27**, 9965–9974 (2019).
- Song, S., Xu, J. & Wang, R. K. Long-range and wide field of view optical coherence tomography for in vivo 3D imaging of large volume object based on akinetic programmable swept source. *Biomed. Opt. Express* **7**, 4734–4748 (2016).
- Sun, J., Timurdogan, E., Yaacobi, A., Hosseini, E. S. & Watts, M. R. Large-scale nanophotonic phased array. *Nature* **493**, 195–199 (2013).
- Hulme, J. et al. Fully integrated hybrid silicon two dimensional beam scanner. *Opt. Express* **23**, 5861–5874 (2015).
- Hutchison, D. N. et al. High-resolution aliasing-free optical beam steering. *Optica* **3**, 887–890 (2016).
- Poulton, C. V. et al. Long-range LiDAR and free-space data communication with high-performance optical phased arrays. *IEEE J. Sel. Top. Quantum Electron.* **25**, 1–8 (2019).
- Poulton, C. V. et al. Coherent solid-state LIDAR with silicon photonic optical phased arrays. *Opt. Lett.* **42**, 4091–4094 (2017).
- Heck, M. J. Highly integrated optical phased arrays: photonic integrated circuits for optical beam shaping and beam steering. *Nanophotonics* **6**, 93–107 (2017).
- Jiang, Y., Karpf, S. & Jalali, B. Time-stretch LiDAR as a spectrally scanned time-of-flight ranging camera. *Nat. Photonics* **14**, 14–18 (2020).
- Okano, M. & Chong, C. Swept Source Lidar: simultaneous FMCW ranging and nonmechanical beam steering with a wideband swept source. *Opt. Express* **28**, 23898–23915 (2020).

26. Klein, T., Wieser, W., Eigenwillig, C. M., Biedermann, B. R. & Huber, R. Megahertz OCT for ultrawide-field retinal imaging with a 1050 nm Fourier domain mode-locked laser. *Opt. Express* **19**, 3044–3062 (2011).
27. Rust, M. J., Bates, M. & Zhuang, X. Sub-diffraction-limit imaging by stochastic optical reconstruction microscopy (STORM). *Nat. Methods* **3**, 793–796 (2006).
28. de Boer, J. F., Leitgeb, R. & Wojtkowski, M. Twenty-five years of optical coherence tomography: the paradigm shift in sensitivity and speed provided by Fourier domain OCT [Invited]. *Biomed. Opt. Express* **8**, 3248–3280 (2017).
29. Gregory, P. A Bayesian revolution in spectral analysis. *AIP Conf. Proc.* **568**, 557–568 (2001).
30. Akinetic All-Semiconductor Technology, <https://www.sweptlaser.com/akinetic-technology> (2020).
31. Izatt, J. A., Choma, M. A. & Dhalla, A.-H. In *Optical Coherence Tomography: Technology and Applications* (eds Wolfgang Drexler & James G. Fujimoto) 65–94 (Springer International Publishing, 2015).
32. Bonesi, M. et al. Akinetic all-semiconductor programmable swept-source at 1550 nm and 1310 nm with centimeters coherence length. *Opt. Express* **22**, 2632–2655 (2014).
33. Behroozpour, B., Sandborn, P. A., Wu, M. C. & Boser, B. E. Lidar system architectures and circuits. *IEEE Commun. Mag.* **55**, 135–142 (2017).
34. Nayar, S. K. & Gupta, M. In *2012 IEEE International Conference on Computational Photography (ICCP)*. 1–11 (IEEE, 2012).
35. Yaqoob, Z., Arain, M. A. & Riza, N. A. High-speed two-dimensional laser scanner based on Bragg gratings stored in photothermorefractive glass. *Appl. Opt.* **42**, 5251–5262 (2003).
36. Chan, T., Myslivets, E. & Ford, J. E. 2-Dimensional beamsteering using dispersive deflectors and wavelength tuning. *Opt. Express* **16**, 14617–14628 (2008).
37. Li, Z., Zang, Z., Han, Y., Wu, L. & Fu, H. Solid-state FMCW LiDAR with two-dimensional spectral scanning using a virtually imaged phased array. *Opt. Express* **29**, 16547–16562 (2021).
38. Tao, Y. K. & Izatt, J. A. Spectrally encoded confocal scanning laser ophthalmoscopy. *Opt. Lett.* **35**, 574–576 (2010).
39. Avnanaki, M. R. et al. Spatial compounding algorithm for speckle reduction of dynamic focus OCT images. *IEEE Photonics Technol. Lett.* **25**, 1439–1442 (2013).
40. Zhou, K. C., Qian, R., Degan, S., Farsi, S. & Izatt, J. A. Optical coherence refraction tomography. *Nat. Photonics* **13**, 794–802 (2019).

Acknowledgements

This work was supported in part by NIH EY028079 (C.V., A.-H. D., J.A.I.), NSF CBET-1902904 (K.C.Z.), and DOD CDMRP W81XWH-16-1-0498 (R.Q.). The authors would like to thank Michael Crawford from Insight Photonics Solution for his assistance in laser setup.

Author contributions

R.Q., K.C.Z., and J.A.I. conceived and developed the idea. R.Q. designed and built the system, analyzed the data. R.Q. and J.Z. collected the data. K.C.Z. developed the theoretical model. R.Q. and A.D. performed the Zemax simulations. C.V. developed the data acquisition software. J.A.I. supervised the work. R.Q. wrote the manuscript with input from all authors.

Competing interests

J.A.I. is an inventor on OCT-related patents filed by Duke University and licensed by Leica Microsystems, Carl Zeiss Meditec, and St Jude Medical. R.Q., K.C.Z., and J.A.I. are inventors on patent application US17/238,521 filed by Duke University that concerns the technology presented in this manuscript. J.Z., C.V., and A.-H.D. declare no competing interests.

Additional information

Supplementary information The online version contains supplementary material available at <https://doi.org/10.1038/s41467-022-29177-9>.

Correspondence and requests for materials should be addressed to Joseph A. Izatt.

Peer review information *Nature Communications* thanks the anonymous reviewer(s) for their contribution to the peer review of this work.

Reprints and permission information is available at <http://www.nature.com/reprints>

Publisher's note Springer Nature remains neutral with regard to jurisdictional claims in published maps and institutional affiliations.



Open Access This article is licensed under a Creative Commons Attribution 4.0 International License, which permits use, sharing, adaptation, distribution and reproduction in any medium or format, as long as you give appropriate credit to the original author(s) and the source, provide a link to the Creative Commons license, and indicate if changes were made. The images or other third party material in this article are included in the article's Creative Commons license, unless indicated otherwise in a credit line to the material. If material is not included in the article's Creative Commons license and your intended use is not permitted by statutory regulation or exceeds the permitted use, you will need to obtain permission directly from the copyright holder. To view a copy of this license, visit <http://creativecommons.org/licenses/by/4.0/>.

© The Author(s) 2022